Complete determination of elastic moduli of interpenetrating metal/ceramic composites using ultrasonic techniques and micromechanical modelling

Siddhartha Roy, Jörg-Martin Gebert, Galyna Stasiuk, Romana Piat, Kay A. Weidenmann, Alexander Wanner

Angaben zur Veröffentlichung / Publication details:

Roy, Siddhartha, Jörg-Martin Gebert, Galyna Stasiuk, Romana Piat, Kay A. Weidenmann, and Alexander Wanner. 2011. "Complete determination of elastic moduli of interpenetrating metal/ceramic composites using ultrasonic techniques and micromechanical modelling." *Materials Science and Engineering: A* 528 (28): 8226–35. https://doi.org/10.1016/j.msea.2011.07.029.

Complete determination of elastic moduli of interpenetrating metal/ceramic composites using ultrasonic techniques and micromechanical modelling

Siddhartha Roy[a,*], Jörg-Martin Gebert[a], Galyna Stasiuk[b], Romana Piat[b], Kay André Weidenmann[a], Alexander Wanner[a]

[a] Institut für Angewandte Materialien – Werkstoffkunde (IAM-WK), Karlsruher Institut für Technologie (KIT), Kaiserstr. 12, 76131 Karlsruhe, Germany
[b] Institut für Technische Mechanik, Karlsruher Institut für Technologie, Kaiserstr. 12, D-76131 Karlsruhe, Germany

1. Introduction

Metal matrix composites (MMC) typically exhibit significantly higher stiffness and in many cases a more pronounced anisotropy in comparison to the corresponding unreinforced metallic matrix [1]. Therefore, measuring the elastic constants of MMCs has great practical significance. Elastic properties of materials can be determined using either static or dynamic techniques [2]. The simplest static technique usually employed is the tensile test, where the Young's modulus is determined from the slope of the linear portion of the stress–strain plot [3]. Dynamic techniques for measurement of elastic properties are usually classified into two groups: resonance methods and methods based on elastic waves [4]. The fundamental difference between static and dynamic techniques arises from the fact that, while static techniques are isothermal, dynamic techniques are adiabatic [3,5]. Dynamic techniques hold an advantage over the static techniques because the stresses used in the former case are far below the elastic limit, and hence they are less prone to effects from irreversible deformation [6]. Furthermore, as the applied infinitesimal stress does not cause any structural changes, repeated measurements can in principle be carried out on the same sample [2]. The scatter shown by the static methods is also significantly higher than the dynamic methods [4,5].

Several authors have studied the relation between static and dynamic elastic constants [7–9]. Landau and Lifshitz [7] proposed a relationship between the static and dynamic Young's moduli using the specific heat at constant pressure and the volume thermal expansivity of the material. Using this relation Ledbetter [5] showed that the two moduli for iron differ by only 0.25% between 0 K and 300 K. A somewhat larger difference between the two moduli has been reported for limestone rocks by Al-Shayea [10]. He summarised results from several studies and showed that ratio of the dynamic and static moduli for limestone rocks lies in the range of 0.85–1.86.

Determination of the elastic properties of MMCs by tensile test has two inherent difficulties. Firstly, in MMCs, at least local permanent deformation resulting from microplasticity or damage initiates at a very early stage during the mechanical test. Hence, the elastic constants determined using this technique are almost always significantly less than their original values [11–13]. Secondly, because of their complex structure, MMCs are often anisotropic. This necessitates elastic constants to be determined along several directions. It is however extremely difficult, if not impossible, to prepare identical MMC samples along different orientations. The number of independent elastic constants in an anisotropic material depends upon the degree of anisotropy (number of independent elastic constants being 2 for isotropy, 3 for

* Corresponding author. Tel.: +49 721 608 42197; fax: +49 721 608 48044.
E-mail address: siddhartha.roy@kit.edu (S. Roy).

cubic, 5 for transverse isotropy and 9 for orthotropy) [14]. Ultrasonic velocity measurements along different directions on a single rectangular parallelepiped sample with edges parallel to the principal orthotropy axes yield 6 out of the 9 elastic constants. To obtain the complete stiffness matrix of a material having orthotropic symmetry, additional sample cuts along specific directions are required [15]. Therefore, this method is destructive since the results cannot be obtained from measurements on a single, retained sample.

Other powerful methods for estimation of the elastic properties of materials with complicated, multiphase microstructure are microstructure modelling using micromechanical and finite element (FE) methods. Different methods can be used for different accuracy levels of the calculations. Very rough guess of the properties can be obtained by Voigt and Reuss bounds, which give the upper and lower bounds for mixtures of the different phases, respectively. The self-consistent (SC), Mori-Tanaka (MT), inverse Mori-Tanaka (IMT) and other methods based on Eshelby solution for single ellipsoidal inclusion give more accurate predictions of the elastic properties. All these methods take into account the shape of the inclusions, their distribution and interaction. Overview of these methods is given in Ref. [16] and the references there in. FE method based calculations give very accurate prediction of the elastic properties and using this method the influence of the irregular shapes of the inclusions can also be introduced in the modelling [17]. However, application of the FE method for complicated microstructure requires large efforts for model creation [18]. In our previous studies on freeze-cast MMCs the comparison of the results obtained by FE, micromechanical and experimental techniques was provided [19–21]. It was shown that the micromechanical models give accurate estimations of the elastic properties and in comparison to FE modelling they are faster and more efficient. Moreover, they require only moderate effort for description of the micro constituent distribution and approximation of their shapes by microstructure characterisation [19,22].

The aim of the current study is to determine the complete stiffness matrices of several metal/ceramic composites having different reinforcement architectures non-destructively and compare them with the results obtained through micromechanical modelling. Two complementary ultrasonic spectroscopic techniques were used in combination for this purpose: ultrasound phase spectroscopy (UPS) and resonant ultrasound spectroscopy (RUS). Few studies have already used these techniques separately to determine the elastic constants of MMCs. UPS was used by Roy and Wanner [23] to determine the longitudinal elastic constants of lamellar MMCs, while Roy et al. [24] used this technique to determine the complete stiffness matrix of interpenetrating MMCs. Until now, RUS has mostly been applied to MMCs reinforced with either particles [25,26] or long fibres [27–29]. An effort has been made in this work to apply both UPS and RUS to determine the complete stiffness matrix of metal/ceramic composites having more complex interpenetrating architecture. Three different composites will be studied: a composite based on freeze-cast ceramic preform, a composite based on open porous ceramic preforms obtained by pyrolysis of cellulose fibres, and a composite based on discontinuous fibre preform. The results will be discussed in light of the thermodynamic constraints for orthotropic symmetry.

In the following the fundamentals of these two experimental techniques and micromechanical modelling are briefly described.

1.1. Ultrasound phase spectroscopy (UPS)

In UPS, continuous and sinusoidal elastic waves are passed through the sample and the phase shift is measured as a function of frequency [30,31]. UPS is an ideal technique to determine sound velocities in samples exhibiting large attenuations due to scattering and internal frictions. A plane monochromatic wave propagating undamped in the x-direction can be written as [32]:

$$u(x, t) = u_0\ e^{i(\omega t + kx)} \tag{1}$$

where $(\omega t + kx)$ is the phase function, $(\omega = 2\pi f)$ is the circular frequency and $(k = 2\pi/\lambda)$ is the wave number. For a specimen of length L_s, the group velocity of a pulse (a pulse being a superposition of many waves) is defined as:

$$V_g = -\frac{2\pi L_s}{(d\Delta\phi/df)} \tag{2}$$

The denominator on the right hand side of Eq. (2) is the slope of the phase–frequency plot. Hence, group velocity is determined by increasing the phase in the specimen of a known length by increasing the frequency, and then finding the slope of the phase–frequency plot. If the plot turns out to be a straight line with a constant slope within a range of frequency, it suggests that the material is non-dispersive in that region. Once V_g for a particular mode (longitudinal or shear with appropriate propagation and polarization vectors) of wave propagation is determined, the corresponding elastic constant C_{ii} is determined according to:

$$C_{ii} = \rho V_g^2 \tag{3}$$

Eq. (3) is valid for non-dispersive materials (phase velocity = group velocity) and it is based on the assumption that the principal axes of orthotropic symmetry are known beforehand and the wave propagation direction and polarization direction are both parallel or perpendicular to these axes. In Eq. (3), ρ is the density, $i = 1$–3 refers to longitudinal elastic constants while $i = 4$–6 corresponds to shear elastic constants. The three longitudinal and the three shear elastic constants of an orthotropic material can be determined using this technique.

Determination of the three off-diagonal elements of the stiffness matrix (C_{12}, C_{13} and C_{23}) of an orthotropic material by this technique is more complicated. Expression for the elastic constant C_{12} is as below [15]:

$$C_{12} = \sqrt{(C_{11} + C_{66} - 2\rho v_{12/12}^2)(C_{22} + C_{66} - 2\rho v_{12/12}^2)} - C_{66} \tag{4}$$

Similar expressions result for C_{13} and C_{23}. In Eq. (4), $\rho v_{12/12}^2$ is the product of the sample density and square of the sound velocity along the face diagonal of the 1–2 plane. As discussed by Gebert et al. [33], the uncertainty in C_{12} results from the uncertainties in C_{11}, C_{22}, C_{66} and $\rho v_{12/12}^2$, and it is typically very high.

1.2. Resonant ultrasound spectroscopy (RUS)

RUS involves the study of the resonant frequencies of solids. These frequencies depend upon the shape, elastic constants, crystallographic orientation or texture, density and dissipation properties of the body. Hence, with this technique the complete stiffness matrix can be obtained non-destructively by measuring the resonant frequencies on a single sample [34,35]. The sample is held lightly between two piezoelectric transducers to ensure a free oscillation of the sample. One transducer applies a sinusoidal excitement to some point on the sample and its resonance response is measured at some other point by the second transducer. A large response is observed when the frequency of the driving transducer corresponds to one of the sample resonant frequencies. Essential to the successful implementation of RUS is the ability to determine the resonant frequencies of a body from its shape, density and the elastic constants (known as forward or direct problem [36]). Once these are computed, carefully constructed fitting algorithms are used to find the moduli from the measured frequencies (known as backward or inverse problem [36]). The procedure to solve the direct

problem is mathematically complicated and its thorough description is outside the scope of this work. A rigorous analysis of this problem as well as the computer algorithm used almost universally is described in detail in the work of Migliori and Sarrao [36]. However, the task of computing the elastic constants analytically from the resonant frequencies has never been undertaken successfully. Instead, a nonlinear optimization procedure has been established. This procedure yields a set of parameters that produces resonant frequencies that are in the best possible agreement with the measured spectra. In order to determine the best possible parameters, a figure of merit, *FOM* is constructed, which provides a measure of how well the calculated and the measured resonance frequencies agree. The *FOM* is defined as:

$$FOM = \sum_{i=1}^{N_p} w_i (f_{calc} - f_{mea})^2 \tag{5}$$

where f_{calc} and f_{mea} are the calculated and the measured resonant frequencies respectively, w_i is a weighting factor chosen based on the confidence of the experimenter for the particular frequency and N_p is the number of resonant frequencies. In the present work, the weighting factor was kept as unity for all the resonant frequencies. As several resonant frequencies depend in almost identical way on some of the elastic constants, hence many more resonances than the total number of parameters to be fit must be measured for a meaningful analysis. Migliori and Sarrao [36] suggest that the number of resonant frequencies measured should ideally be at least 5 times the number of parameters to be determined. Furthermore, the sample for RUS must have very well defined geometry with regards to face parallelism – a few microns per mm – and the sample needs to be perfectly rectangular. Above conditions being fulfilled and using a reasonably good guess for the input parameters, error bars for compressional moduli in the range of 0.5–1.0%, for shear moduli in the range of 0.02% and for off–diagonal moduli in the range of 2–3% are achievable [36].

1.3. Micromechanical modelling using Mori-Tanaka model (MT)

The MT model is a very efficient method utilized for modelling of the microstructure with "ellipsoid"-like inclusions [19]. Combination of the MT method [37] with averaging procedure [38] allows calculating the effective stiffness of a two phase material in the following form:

$$\mathbf{C}^{MT} = \mathbf{C}^{M} + f_I\{(\mathbf{C}^{I} - \mathbf{C}^{M}) : \mathbf{T}\} : ((1 - f_I)\mathbf{I} + f_I\{\mathbf{T}\})^{-1} \tag{6}$$

with Wu-tensor [39]

$$\mathbf{T} = \mathbf{C}^{M} + (\mathbf{I} + \mathbf{S} : (\mathbf{C}^{M})^{-1} : (\mathbf{C}^{I} - \mathbf{C}^{M}))^{-1} \tag{7}$$

where $\mathbf{C}^M$ and $\mathbf{C}^I$ are stiffness tensors of the first (matrix) and the second (inclusions) phases, respectively. f_I is the volume fraction of the inclusions and $\mathbf{I}$ is the fourth order identity tensor. Eshelby tensor $\mathbf{S}$ depends on the shape of the inclusion and elastic properties of the matrix. Different forms of the $\mathbf{S}$ tensor are used for different kinds of inclusion geometry [40]. Curly brackets $\{\cdot\}$ denote averaging over all possible directions.

The 3D averaging $\{\ \}$ in Eqs. (6) and (7) is provided using two Euler angles for random distribution using

$$\{C_{ijkl}\} = \frac{1}{4\pi}\int_0^{2\pi}\int_0^{\pi} a_{ip}a_{jq}a_{kr}a_{js}C_{pqrs}\,\sin\theta\,d\theta\,d\varphi \tag{8}$$

where a_{ij} are the components of the transformation matrix:

$$\begin{pmatrix} \cos\ \theta\cos\varphi & -\sin\varphi & \sin\theta\cos\varphi \\ \cos\theta\sin\varphi & \cos\varphi & \sin\theta\sin\varphi \\ -\sin\theta & 0 & \cos\theta \end{pmatrix} \tag{9}$$

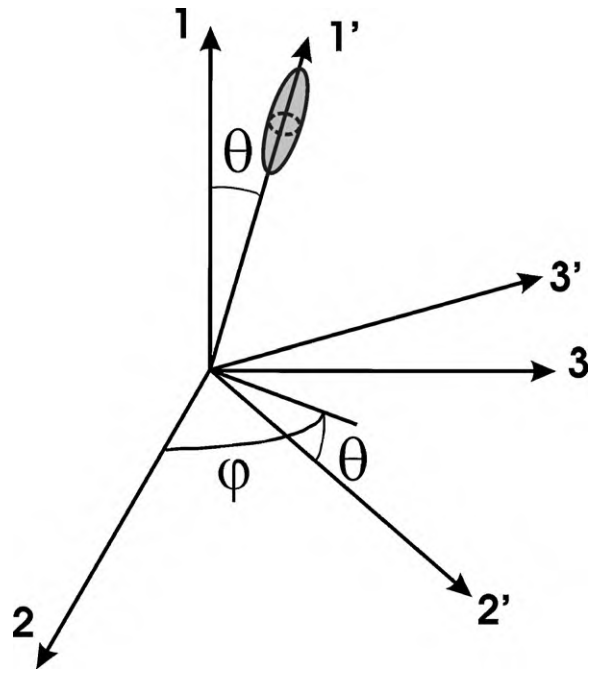

Fig. 1. Euler angles in relation to the local 1′, 2′, 3′ and global 1, 2, 3 co-ordinate systems [38] for inclusions with circumferential symmetry around 1′.

Definition of the Euler angles is given in Fig. 1. For averaging procedure only in 2–3 plane Eq. (8) will change to

$$\{C_{ijkl}\} = \frac{1}{2\pi}\int_0^{2\pi} a_{ip}a_{jq}a_{kr}a_{js}C_{pqrs}\,d\varphi \tag{10}$$

and components of a_{ij} are the components of

$$\begin{pmatrix} \cos\ \varphi & -\sin\varphi & 0 \\ \sin\varphi & \cos\varphi & 0 \\ 0 & 0 & 1 \end{pmatrix} \tag{11}$$

In the next sections this theoretical background was utilized for modelling of the studied composites.

2. Experimental procedure and microstructure modelling

2.1. Specimen material

Three different metal/ceramic composites fabricated by squeeze-casting aluminum based alloys in different alumina preforms were investigated. The preforms had different alumina content and their processing methods were different. The production routes for the three composites had only one common principal axis, the direction of squeeze-casting. Hence, transverse isotropic symmetry with respect to this direction is expected. However, due to the limited sample volume, the randomness in the transverse plane could be compromised, resulting in complex, non-symmetric sample properties.

Processing routes of the studied composites are briefly described in the following:

2.1.1. Composite based on freeze-cast alumina preforms (sample A)

The composite was fabricated by squeeze-casting AlSi12 melt in freeze-cast alumina preform. The preform was fabricated at Institut für Keramik im Maschinenbau (IKM) at Karlsruher Institut für Technologie (KIT), Germany, via freeze-casting of a ceramic suspension, freeze-drying and subsequent sintering [41]. Freeze-casting

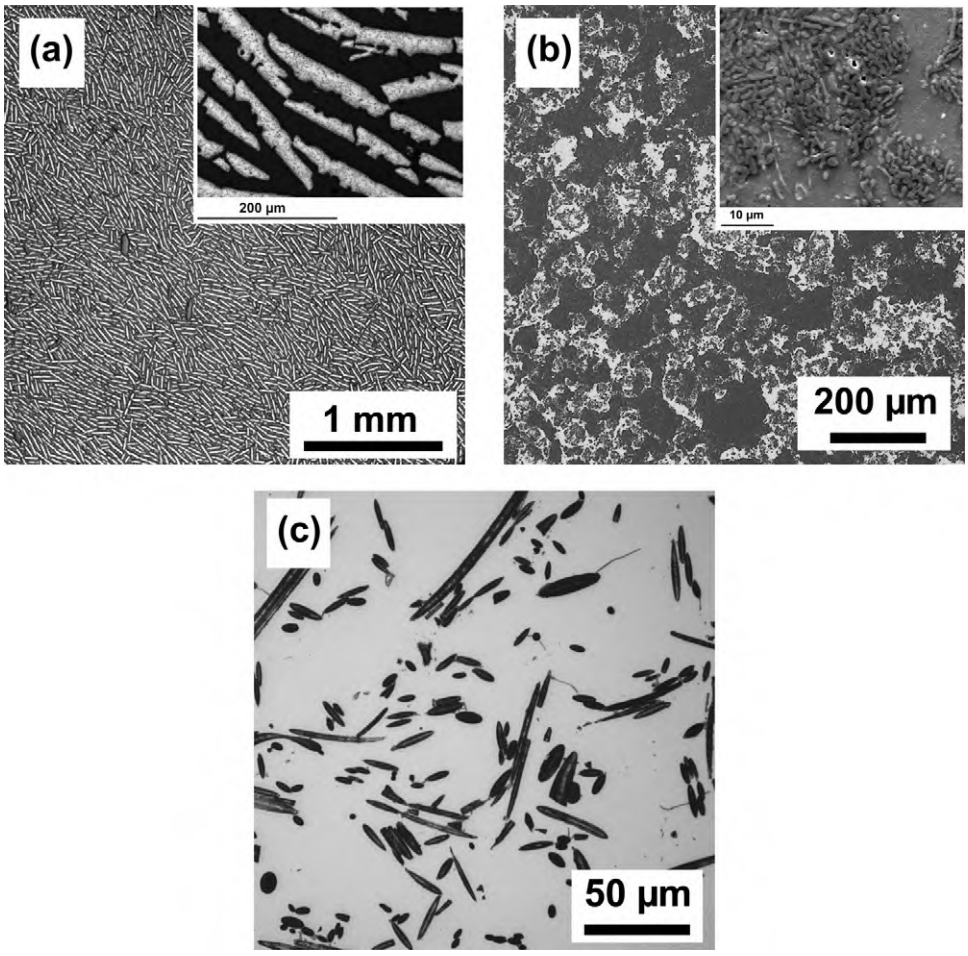

Fig. 2. Typical light optical micrographs of the three composites: (a) micrograph of sample A for the face perpendicular to the freezing direction, (b) micrograph of sample B for the face perpendicular to the direction of preform pressing and squeeze-casting and (c) micrograph of sample C for the face perpendicular to the direction of squeeze-casting. In these micrographs the ceramic phase is dark, while the metallic alloy is brighter. The inset of (a) shows a zoomed-in view of the typical lamella structure of sample A. Inset of (b) shows typical scanning electron micrograph of the sample B.

was carried out at −30 °C. Freeze-cast preforms were subsequently infiltrated by squeeze-casting at the Institute of Surface Technology and Materials Science at Aalen University of Applied Sciences, Germany. The composite was fabricated in the form of a plate with nominal dimensions of 10 mm × 44 mm × 66 mm. The sample studied in this work was cut in the form of a rectangular parallelepiped from this plate using a diamond coated steel wire saw and further polished until required degree of surface finish was attained. Typical optical microstructure of the composite for the face perpendicular to the freezing direction is shown in Fig. 2a. The inset of this figure shows the lamella structure of the composite at a higher magnification. The microstructure consists of several domains, within which the alternating ceramic and the metallic alloy lamellae are arranged in parallel. The lamella spacing and the domain size are functions of freeze-casting parameters. Co-ordinate system used for the sample is shown in Fig. 3, with direction 1 being parallel to the direction of freeze-casting and squeeze-casting. Mass and dimensions of the sample, as well as its density calculated there from are mentioned in Table 1. Nominal ceramic volume content was calculated from the measured density, assuming absence of porosity.

Detail characterisation of the lamellar structure for micromechanical modelling is discussed in Ref. [42]. The lamellae were approximated as ellipses using a self written software code [22]. Ratio of the small and large half axes of the ellipses determined this way lied in the range of 0.096 and 0.3 with a mean value 0.15. For modelling purpose the microstructure was assumed not to change along the freezing-direction, thereby converting it into a 2D problem. Eqs. (6), (7), (10) and (11) were utilised for calculation of the effective elastic properties of the composite. The metallic alloy and the ceramic phase of the composite were assumed to be isotropic and Eshelby tensor for elliptical cylinders was employed [40]. Isotropic elastic properties of alumina and AlSi12 were used for model calculations. The Young's modulus and the shear modulus of AlSi12 were determined in an earlier study to be 80 GPa and 30 GPa [23], while the Young's modulus and Poisson's ratio of alumina were taken as 390 GPa [43] and 0.24 [44], respectively. Model calculations were carried out for minimal, maximal and

Table 1
Mass and dimensions of individual samples. Density and nominal ceramic volume content of each sample have been calculated from the measured mass and dimensions.

Sample	l_1 (mm)	l_2 (mm)	l_3 (mm)	Mass (g)	Density (Mg m^{-3})	Ceramic volume content
A	5.22	5.44	5.90	0.54033	3.227	47%
B	9.25	6.78	6.35	1.2378	3.112	37%
C	7.02	5	6	0.5872	2.788	10%

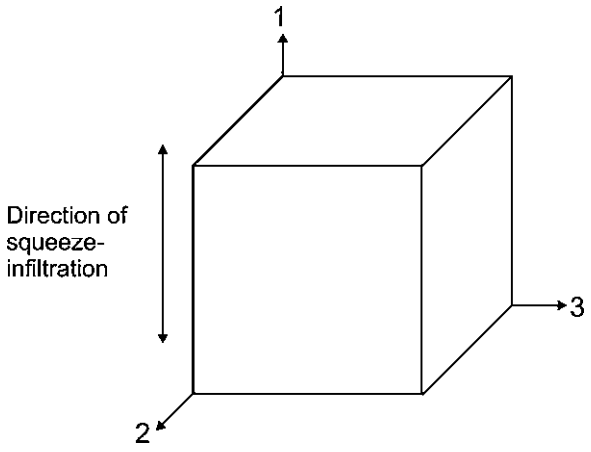

Fig. 3. Co-ordinate system used for the three MMC samples. In all three samples the squeeze-casting was carried out along direction 1. In sample A, direction of freeze-casting and squeeze-casting were same. In sample B, direction of preform pressing and squeeze-casting were same.

mean aspect ratios of the lamella half axes and for the actual ceramic volume fraction mentioned in Table 1.

2.1.2. Composite based on open porous ceramic preforms obtained by pyrolysis of cellulose fibres (sample B)

The composite was fabricated by the Materials Research Team of Aalen University of Applied Sciences, Germany, following a processing route thoroughly described in Ref. [45]. The mechanism of internal load transfer in this composite under external tension and compression has already been studied in an earlier work [46]. Commercially available alumina powder was mixed with cellulose fibres used as pore forming agent. After mixing, the powder mixture was uni-directionally pressed into plates having nominal dimensions of 10 mm × 44 mm × 66 mm. The plates were subsequently sintered at 1550 °C in an oxidising atmosphere. Pyrolysis of the pore forming agents took place during sintering process. The porous preforms were subsequently infiltrated with AlSi12 via squeeze-casting along the same direction as that of preform pressing. The studied sample was cut in the form of a rectangular parallelepiped from this composite plate using a diamond coated steel wire saw and further polished until required degree of surface finish was attained. Co-ordinate system used for the sample is shown in Fig. 3, with direction 1 being parallel to the direction of preform pressing and squeeze-casting. Fig. 2b shows typical optical micrograph of the sample for the face perpendicular to direction 1. Mass and dimensions of the sample, as well as its density calculated there from are mentioned in Table 1. Nominal ceramic volume content was calculated from the measured density assuming absence of porosity. Inset of Fig. 2b shows the scanning electron micrograph of the composite. Only few micro pores are observed within the ceramic walls. These micro pores may generate due to differential thermal contraction between the two phases during cool-down after melt infiltration and their presence may shift the ceramic content of the composite to about 0.7 vol% higher [46]. The micrograph shows that the alumina particles are prolate ellipsoids in shape. Aspect ratios between the small and large half axes of the ellipsoids were measured and they lied in the range of 0.2 and 0.63 with a mean value of 0.3.

Micromechanical modelling of the composite was carried out using the 3D model described in Eqs. (6)–(9). For the inclusions the Eshelby tensor was calculated using the formulae for prolate ellipsoids [40] and the isotropic elastic constants of alumina and AlSi12.

2.1.3. Composite based on discontinuous fibre preform (sample C)

The short fibre reinforced composite studied in this work was fabricated at Mahle GmbH, Stuttgart, Germany by squeeze-casting. Commercial purity Al was used as the metallic matrix, while 10 vol% discontinuous Al_2O_3 fibres (Saffil® by ICI) were used as the reinforcement. For thorough description of the composite, we refer to Ref. [47]. Fig. 2c shows the microstructure of the composite for the face perpendicular to the direction of squeeze-casting. The sample was cut in the form of a rectangular parallelepiped. Co-ordinate system used for the sample is shown in Fig. 3, with direction 1 being parallel to the direction of squeeze-casting. Mass and dimensions of the sample, as well as its density calculated there from are mentioned in Table 1.

Micromechanical modelling of the composite material was carried out using the 3D model (Eqs. (6)–(9)). Two different fibre distributions were utilised: The first one is random in plane 2–3 and the second one is random in the whole 3D space. For the inclusions the Eshelby tensor was calculated using the formulae for prolate ellipsoids [40]. Isotropic elastic constants of alumina and Al were used for the modelling purpose. The Young's modulus and Poisson's ratio of Al were taken as 70 GPa and 0.34 [48], respectively. Model calculations were carried out for a fibre volume content of 10% and mean aspect ratio (small half axis/long half axis) of 0.125.

2.2. Ultrasound phase spectroscopy (UPS)

UPS was used to determine the three longitudinal and the three shear elastic constants. The measurements were accomplished using an electronic network analyser (Advantest, model R3754A) and two identical broadband piezoelectric transducers (Panametrics, model V122 with nominal central frequency 7.5 MHz and diameter 9.5 mm for longitudinal elastic constants and model V155 with nominal central frequency 5 MHz and diameter 12.7 mm for shear elastic constants). These transducers were attached to opposite sides of the rectangular parallelepiped samples using a water-soluble couplant. First, measurements were carried out with the same pair of transducers (V122 or V155) in contact to each other with only the couplant to determine the phase response of the experimental system. This phase response was subtracted from each subsequent measurement with the sample to determine the phase shift caused only by the sample. The phase as well as the magnitude ratio (referred to as amplitude) between the input and output electronic signals were measured for each data point (1201 data points per measurement). For longitudinal elastic constants, the phase and amplitude spectra were recorded in the frequency range from 10 kHz to 15 MHz; while for shear elastic constants the same range was from 10 kHz to 10 MHz. The slope of the phase versus frequency plot was determined by linear regression in such a way, that both the frequency and the frequency range were as high as possible. This way, the detrimental influence of the side wall reflections, which typically occur at low frequencies [31], may be overcome. Two different shear wave velocities were calculated for each shear elastic constant. For the shear elastic constants C_{44}, C_{55} and C_{66}, the shear wave velocities were V_{23} and V_{32}, V_{13} and V_{31} and V_{12} and V_{21}; respectively. In all samples and for each shear elastic constant, the respective shear wave velocities were similar, suggesting that the samples had orthotropic or higher symmetry [32]. Average of the two corresponding shear wave velocities was used to determine the respective shear elastic constants.

2.3. Resonant ultrasound spectroscopy (RUS)

For RUS, the samples were assumed to have orthotropic symmetry, having 9 independent elastic constants. The three longitudinal and the three shear elastic constants for each sample determined by UPS were used as input for RUS. However, with UPS it was not pos-

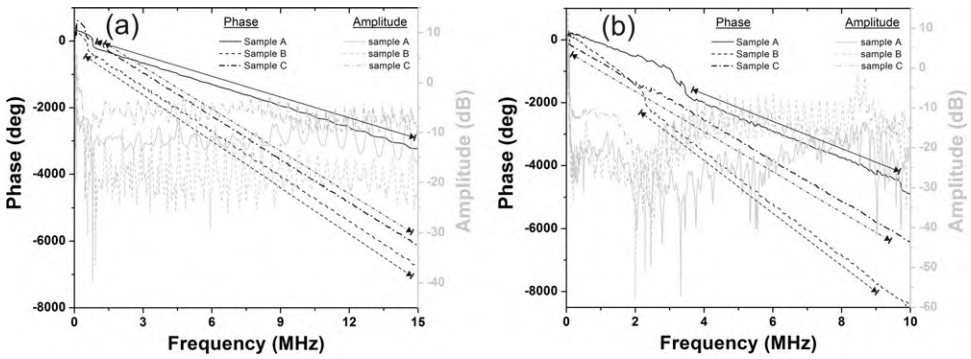

Fig. 4. Typical phase and amplitude spectra obtained for (a) longitudinal and (b) shear elastic constants using ultrasound phase spectroscopy (UPS).

sible to determine the three off-diagonal elastic constants (C_{12}, C_{13} and C_{23}) non-destructively. Hence, initial guesses were necessary for them, in order to determine the expected resonant frequencies of the samples using the forward calculation. For sample A, these three elastic constants were estimated based on the theory of uni-directionally fibre reinforced composites (the expressions to calculate the elastic constants of a uni-directionally fibre reinforced composite are summarised by Berthelot [49]) and using the elastic constants of isotropic alumina and AlSi12; while for samples B and C, they were calculated from the already determined longitudinal and shear elastic constants assuming isotropy. To determine the actual resonant frequencies, the samples were placed along its body diagonal between two identical transducers attached to a very rigid stage. The complete stage along with the transducers was manufactured by Quasar (Quasar International Inc., New Mexico, USA). The same network analyzer used for UPS was used to generate the input signal and to record the output signal. A wideband, high speed amplifier (model BA4825 from NF Corporation, Yokohama, Japan) was used to amplify the signal to the input transducer. Phase and amplitude were measured for each swept frequency. For each sample, the first 50 resonant frequencies were determined from the amplitude spectra. At least four measurements were carried out along different body diagonals of each sample. This was done to minimise the number of missed resonant frequencies. The measured resonant frequencies as well as the mass and dimensions of each sample were put as input to back calculate the elastic constants.

3. Results

Fig. 4 shows typical phase and amplitude spectra for the three MMC samples. Phase and amplitude spectra for longitudinal elastic constants are shown in Fig. 4a, while the spectra for shear elastic constants are shown in Fig. 4b. The trend shown by the longitudinal spectra in the three samples are similar. Apart from regular local oscillations due to residual standing waves, the phase spectra are linear with a constant slope over almost the complete frequency range. This suggests that the samples are non-dispersive and the velocity determined from the slope (following Eq. (2)) is independent of frequency. The amplitude spectra oscillate in a complex manner and always remain within the measurable range. Experience shows that the signal becomes non-measurable when the amplitude typically drops below approx. −40 dB in the amplitude spectrum [50]. The spectra for shear waves show a more complex behavior. As shown in Fig. 4b, several shear wave phase spectra showed two linear regions separated by a non-linear region. This is visible in the phase spectra of samples A and B at around 2.5–3 MHz. Corresponding amplitude spectra also showed drastic drops in this range. The slopes of the two linear regions in each spectrum are similar to each other. As already mentioned, the detrimental influence of the side wall reflections is attenuated at higher frequencies, and hence, shear wave velocities were calculated from the slopes of the linear regions at higher frequency range. The range of frequency used to calculate the shear wave velocity is marked in each spectrum in Fig. 4. Within this marked frequency range each spectrum has a constant slope, suggesting that even the shear wave is non-dispersive and the group velocity is equal to phase velocity [31]. The longitudinal and the shear elastic constants were determined following Eq. (3), using the longitudinal and shear wave velocities and the density of each sample. These longitudinal and the shear wave velocities, as well as the corresponding elastic constants for the three MMC samples are listed in Table 2.

Fig. 5 shows the RUS spectra for the three MMC samples. Resonant frequencies were determined from the peak positions. Tables 3–5 show the results obtained by fitting the experimentally measured resonant frequencies to the code written by Migliori and Sarrao [36] based on the input values of the elastic constants and sample mass and dimensions. Fit obtained for only the first 20 resonant frequencies for each sample are shown here. The column headers in these tables have the following meanings: n corresponds to the number of the resonant peak, f_{ex} and f_r are the measured and the fitted frequencies (in MHz) and $\%err$ is the error in fitting that particular peak. Table 6 shows the summary of the elastic constants obtained from RUS for first 50 resonant frequencies for each sample, and their comparison with elastic constants measured via UPS. The rms errors in % between the calculated and the measured resonant frequencies for each sample are also shown in the table. The compliance matrix of each MMC sample was determined by inverting the obtained stiffness matrix and the engineering elastic constants (Young's modulus (E), Poisson's ratio (ν) and shear elastic constant (G)) were computed there from. These engineering elastic constants for each MMC sample are listed in Table 7.

Table 2
Longitudinal and shear wave velocities for the three MMC samples determined via UPS. The longitudinal and the shear elastic constants were determined using the respective sound wave velocities and the density of each sample.

Sample	V_{11} (m/s)	V_{22} (m/s)	V_{33} (m/s)	Avg. V_{32} and V_{23} (m/s)	Avg. V_{13} and V_{31} (m/s)	Avg. V_{12} and V_{21} (m/s)	C_{11} (GPa)	C_{22} (GPa)	C_{33} (GPa)	C_{44} (GPa)	C_{55} (GPa)	C_{66} (GPa)
A	8657	7621	8141	4416	4834	4326	242	188	214	64	76	61
B	7608	7922	7892	4413	4212	4186	181	196	194	61	55	55
C	6519	6570	6547	3362	3354	3229	119	120	120	32	31	29

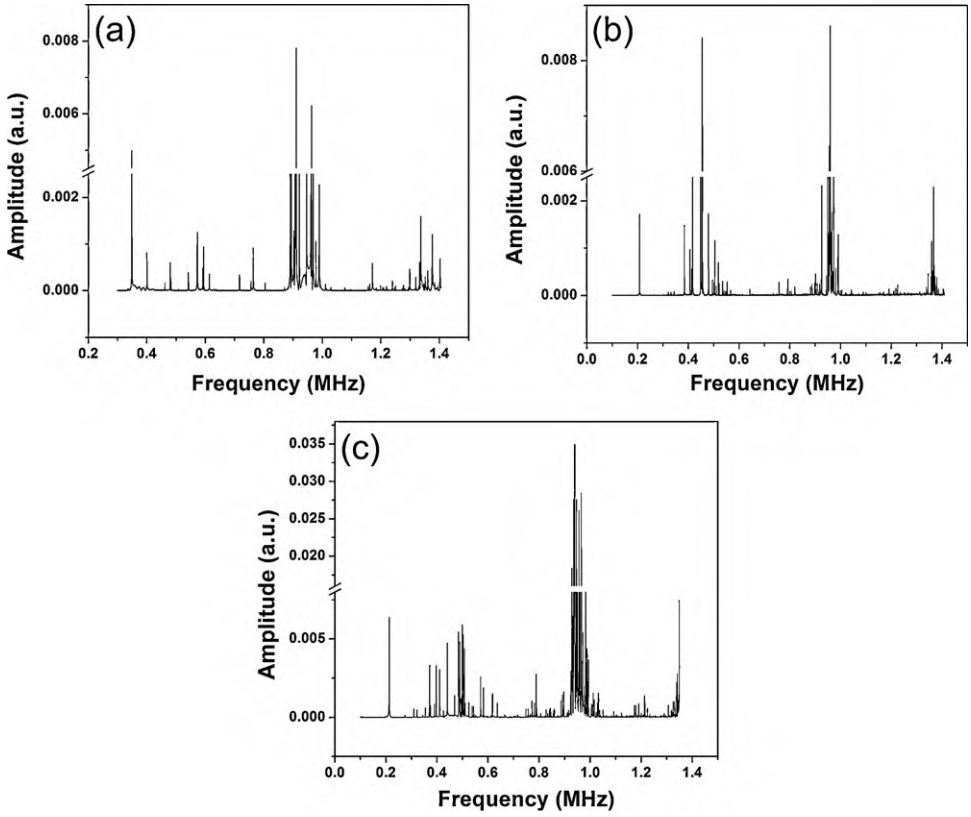

Fig. 5. RUS spectra for the three MMC samples: (a) Sample A, (b) Sample B and (c) Sample C.

Comparison between the complete stiffness matrices determined using experimental and numerical techniques for the three composite samples is shown in Table 8. Fig. 6 shows the variation of the elastic constant C_{33} with ceramic content in sample B for different half axis aspect ratios ranging from spherical (ratio = 1) to fibre-like (ratio = 0.01). The experimentally obtained result is also shown in the same plot. A zoomed in view of the plot at ceramic contents relevant to the actual sample is also shown in the right hand side plot of Fig. 6. Correlation between the half-axis aspect ratio (shape) of the inclusions and the elastic constant C_{33} (or C_{22}) for random distribution of the particles in 2–3 plane is clearly recognizable: a decreasing half-axis aspect ratio corresponds to an increase in the elastic constant. Good correspondence between calculated (for mean aspect ratio) and measured elastic constant is also visible.

4. Discussions

Table 6 shows that in all cases the elastic constants determined by UPS show very good reproducibility also in RUS (maximum deviations between the elastic constants determined by the two techniques lie in the range of 6–7%). The values of the rms errors are however considerably higher than that suggested by Migliori

Table 3
Comparison between experimentally obtained and fitted resonant frequencies for the first 20 resonant peaks obtained from RUS on sample A.

n	f_{ex} (MHz)	f_r (MHz)	%err
1	0.349025	0.347033	−0.57
2	0.400843	0.403743	0.72
3	0.462155	0.463939	0.39
4	0.480615	0.481898	0.27
5	0.483008	0.489053	1.25
6	0.507935	0.515612	1.51
7	0.52804	0.524268	−0.71
8	0.540227	0.5354	−0.89
9	0.542548	0.5404	−0.4
10	0.5728	0.567331	−0.95
11	0.591845	0.590179	−0.28
12	0.594373	0.593917	−0.08
13	0.614453	0.614438	0
14	0.629977	0.62601	−0.63
15	0.637033	0.637101	0.01
16	0.661293	0.668026	1.02
17	0.69036	0.688507	−0.27
18	0.6944	0.690852	−0.51
19	0.69905	0.69541	−0.52
20	0.717398	0.722718	0.74

Table 4
Comparison between experimentally obtained and fitted resonant frequencies for the first 20 resonant peaks obtained from RUS on sample B.

n	f_{ex} (MHz)	f_r (MHz)	%err
1	0.208163	0.207127	−0.5
2	0.265602	0.265423	−0.07
3	0.271953	0.273214	0.46
4	0.322	0.322133	0.04
5	0.332272	0.335121	0.86
6	0.343692	0.343974	0.08
7	0.344511	0.344547	0.01
8	0.38444	0.384886	0.12
9	0.406725	0.409722	0.74
10	0.412721	0.414928	0.53
11	0.414536	0.416352	0.44
12	0.41696	0.417609	0.16
13	0.417397	0.418769	0.33
14	0.448778	0.448662	−0.03
15	0.455179	0.455239	0.01
16	0.455905	0.45842	0.55
17	0.479924	0.480613	0.14
18	0.495764	0.495448	−0.06
19	0.501799	0.500684	−0.22
20	0.504167	0.507031	0.57

Table 5
Comparison between experimentally obtained and fitted resonant frequencies for the first 20 resonant peaks obtained from RUS on sample C.

n	f_{ex} (MHz)	f_r (MHz)	%err
1	0.21315	0.20958	−1.67
2	0.27483	0.276698	0.68
3	0.29488	0.296731	0.63
4	0.31026	0.305313	−1.59
5	0.32232	0.322545	0.07
6	0.34411	0.347127	0.88
7	0.35443	0.349113	−1.5
8	0.36942	0.370292	0.24
9	0.37185	0.371199	−0.17
10	0.37481	0.372555	−0.6
11	0.39028	0.390733	0.12
12	0.39732	0.39637	−0.24
13	0.41125	0.410792	−0.11
14	0.42607	0.426323	0.06
15	0.44081	0.438723	−0.47
16	0.46943	0.471476	0.44
17	0.4852	0.486326	0.23
18	0.48996	0.490378	0.09
19	0.4947	0.496288	0.32
20	0.49707	0.497899	0.17

and Sarrao [36] (they suggest a value in the range of 0.1–0.2% for a very good measurement with a very well prepared sample). This relatively high rms error may be attributed to the complex microstructure of the MMCs, inhomogeneities inherent in the composite sample used and difficulty in preparing samples having ideal rectangular parallelepiped geometry. Due to the above-mentioned inherent difficulties of applying RUS in MMCs, earlier studies have also reported rms errors in the same range as obtained in this work [26,27]. Presence of inhomogeneities is known to significantly affect the quality of the fit obtained in RUS. Kaplan et al. [51] have shown that when the length scale of the inhomogeneity is approximately 15% of the smallest dimension of the sample, the fit obtained in RUS gets significantly affected. The optical micrographs of Fig. 2 however show that the sizes of the reinforcements (when considered as inhomogeneity in the MMC) are significantly less than this limit. The MMC samples can therefore be considered as homogeneous for RUS measurement.

Table 8 shows that very good correlation exists among the elastic constants determined using experimental and numerical techniques. Due to the different reinforcement architectures the degree of anisotropy in the three composite samples is different. While the behavior of sample A is orthotropic, samples B and C are mostly isotropic.

In sample A, the highest stiffness is observed along the freezing direction of the ceramic preform. This is caused by the mostly continuous ceramic lamellae oriented along the freezing direction. Stiffness along directions 2 and 3 strongly depend upon the size and orientation of the individual domains. Previous analysis has already shown that individual domains display a pronounced elastic [19,23] and elastic–plastic [52] anisotropy. In a single domain composite sample with domain orientation 0° with direction 2, $C_{22} \approx C_{11}$, with C_{33} being significantly lower. If the length scale of the sample is much larger than the domain size and the domains are randomly oriented, stiffness along directions 2 and 3 should be similar and the symmetry of the sample should be transversely

Table 6
Summary of the elastic constants obtained from RUS for first 50 resonant frequencies, and their comparison with elastic constants measured via UPS.

Sample	rms error (%)	C_{11} (GPa)	C_{22} (GPa)	C_{33} (GPa)	C_{23} (GPa)	C_{13} (GPa)	C_{12} (GPa)	C_{44} (GPa)	C_{55} (GPa)	C_{66} (GPa)
A										
Input	0.5825	242	188	214	90	85	85	64	76	61
Final		257	200	203	79	65	90	62	74	65
B										
Input	0.5779	181	196	194	76	76	76	61	55	55
Final		188	195	191	80	78	84	57	55	55
C										
Input	0.6529	119	120	120	58	58	58	32	31	29
Final		120	124	112	57	56	62	30	32	33

Table 7
Engineering elastic constants of the three MMC samples determined from the stiffness matrix.

Sample	E_{11} (GPa)	E_{22} (GPa)	E_{33} (GPa)	G_{23} (GPa)	G_{31} (GPa)	G_{12} (GPa)	ν_{21}	ν_{31}	ν_{12}	ν_{32}	ν_{13}	ν_{23}
A	211	152	168	62	74	65	0.274	0.136	0.382	0.334	0.171	0.301
B	140	145	146	57	55	55	0.329	0.287	0.318	0.287	0.275	0.285
C	80	83	77	30	32	33	0.364	0.309	0.353	0.305	0.321	0.327

Table 8
Correlation between experimentally measured and theoretically calculated elastic constants for the three composite samples.

in GPa	Sample A				Sample B				Sample C		
	Experiment	Calculated for axes ratio			Experiment	Calculated for axes ratio			Experiment	Calculated for mean axes ratio 0.125	
		Mean 0.15	Min 0.1	Max 0.3		Mean 0.3	Min 0.2	Max 0.63		2D random	3D random
C_{11}	257	271	271	272	188	174	176	173	120	119	122
C_{22}	200	203	199	208	195	187	182	192	124	125	122
C_{33}	203	203	199	208	191	187	182	192	112	125	125
C_{23}	79	87	86	88	80	79	78	80	57	61	60
C_{13}	65	81	80	82	78	77	77	76	56	59	60
C_{12}	90	81	80	82	84	77	77	76	62	59	60
C_{44}	62	58	56	59	57	54	52	55	30	32	31
C_{55}	74	65	61	67	55	50	51	50	32	30	31
C_{66}	65	65	61	67	55	50	51	50	33	30	31

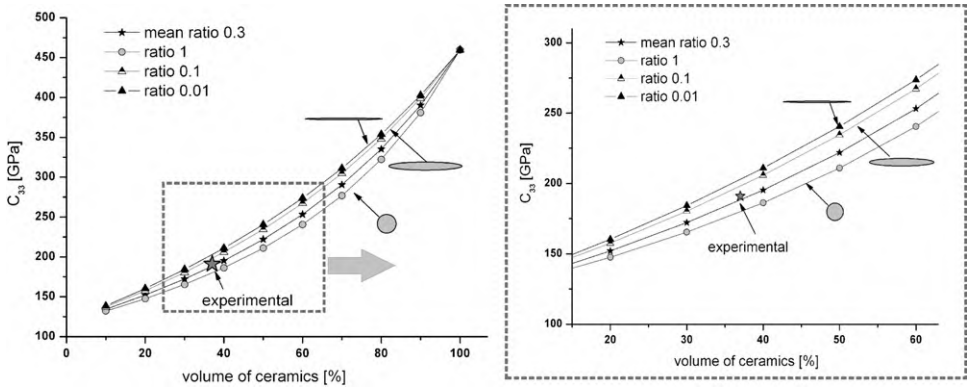

Fig. 6. Variation of the elastic constant C_{33} with ceramic volume fraction corresponding to sample B. Effect of the aspect ratio of the inclusions on the elastic constant is shown. The right hand side plot shows a zoomed in view of the plot for ceramic contents relevant to the actual sample.

isotropic. However, due to the finite domain size and non-random domain distribution in the 2–3 plane of the actual sample, stiffness along directions 2 and 3 differ marginally. Comparison of the experimental results with the results from numerical modelling with mean half-axes ratio shows very good match for the longitudinal elastic constants C_{22} and C_{33}. However, for the elastic constant C_{11}, the numerical prediction is approximately 5% more than the experimental value. This can be attributed to the fact that for numerical modelling the microstructure was assumed to remain unchanged along the freezing direction. However, as has already been shown in Ref. [23], the real microstructure was more complex and consisted of irregularities like inclined lamella orientation, discontinuity along the freezing direction, etc. These irregularities reduce the stiffness of the real microstructure along the freezing direction.

Good match is also obtained for remaining main diagonal elements of the stiffness matrix.

Because of the mostly random distribution of the reinforcement, the sample B behaves almost as an isotropic material. In sample B, C_{11} is marginally less than C_{22} and C_{33}. This results from preform pressing prior to sintering along direction 1 [24]. Apart from the elastic constant C_{11}, for all other elements of the stiffness matrix very good match is obtained between experiment and numerical modelling. The experimentally determined C_{11} is about 5% higher than the numerical prediction. In the theoretical model the distribution of the ceramic particles has been assumed to be random in the 2–3 plane, with the direction 1 being transverse to this plane. Although preform pressing prior to sintering introduces preferred orientation of the particles in the 2–3 plane, due to the interpenetrating structure, stiffness along direction 1 would be enhanced significantly in comparison to a complete in plane particle distribution.

In sample C the assumption of a complete in-plane distribution of fibres in the 2–3 plane contradicts the experimental results. In such a case the elastic constants C_{22} and C_{33} should be similar. However, the experimental results show approximately 10% deviation between them. In fact, the experimentally determined values of C_{11} and C_{22} are similar. Table 8 shows that the numerical predictions from both 2D random and 3D random assumptions are similar, however, when all the elements of the stiffness matrix are considered, the assumption of 3D random distribution gives marginally better match with experiment. These results show that short fibres are not perpendicular to the direction 1 but they are partially inclined to this direction.

Lemprier [53] have generalized the thermodynamic constraints on the values of the engineering elastic constants of an orthotropic material. These conditions are further summarised in Ref. [54]. Following conditions must be fulfilled:

(i) The sum of the work done by all the stresses must be positive in order to avoid generation of energy. As work done is determined by the diagonal elements of the stiffness matrix, these elements must be positive. In other sense:

$$C_{11}, C_{22}, C_{33}, C_{44}, C_{55}, C_{66} > 0$$

(ii) For the stiffness matrix to be positive definite, the determinant of the matrix must be positive.

(iii) The Poisson's ratios and the Young's moduli must fulfil the condition:

$$\frac{\nu_{ij}}{E_{ii}} = \frac{\nu_{ji}}{E_{jj}}$$

Table 6 shows that the above-mentioned first condition is fulfilled in all three MMC samples. Conditions (ii) and (iii) for the three MMC samples are summarised in Table 9. It clearly shows that in all three samples the determinants of the stiffness matrices are positive. Additionally, the correlation between Poisson's ratios and Young's moduli also hold within slight uncertainties.

In case of sample A, Young's modulus along the three main directions follow the relationship $E_{11} > E_{33} > E_{22}$, and accordingly, from the above mentioned condition (iii) the Poisson's ratios should follow the relations $\nu_{12} > \nu_{21}$, $\nu_{13} > \nu_{31}$ and $\nu_{32} > \nu_{23}$, respectively. Table 7 shows that these conditions are indeed fulfilled. In each of the two samples B and C the Young's moduli along the three principal directions are close to each other and hence the Poisson's ratios are also similar to each other.

Table 9
The condition of orthotropy in the three MMC samples.

Sample	Determinant of stiffness matrix	$\frac{\nu_{12}}{E_{11}}$	$\frac{\nu_{21}}{E_{22}}$	$\frac{\nu_{13}}{E_{11}}$	$\frac{\nu_{31}}{E_{33}}$	$\frac{\nu_{23}}{E_{22}}$	$\frac{\nu_{32}}{E_{33}}$
A	2.167×10^{12}	1.81×10^{-3}	1.803×10^{-3}	8.104×10^{-4}	8.095×10^{-4}	1.98×10^{-3}	1.988×10^{-3}
B	7.437×10^{11}	2.27×10^{-3}	2.27×10^{-3}	1.96×10^{-3}	1.97×10^{-3}	1.97×10^{-3}	1.97×10^{-3}
C	2.703×10^{10}	4.41×10^{-3}	4.39×10^{-3}	4.01×10^{-3}	4.01×10^{-3}	3.94×10^{-3}	3.96×10^{-3}

5. Conclusions

Complete stiffness matrices of three different composite samples with complex interpenetrating microstructures were determined non-destructively by combining ultrasound phase spectroscopy and resonant ultrasound spectroscopy. The composites had similar matrix and reinforcement, but the reinforcement architecture differed. The three longitudinal and the three shear elastic constants of the samples were first determined using ultrasound phase spectroscopy. These measured elastic constants were further used to determine the complete stiffness matrix of each sample using resonant ultrasound spectroscopy and assuming orthotropic symmetry. Six of the nine elastic constants were predetermined by ultrasound phase spectroscopy and used as initial guess input for resonant ultrasound spectroscopy analysis, making the final results of all nine elastic constants more reliable. Although all three composite samples had only a single principal axis, due to the limited sample volume the randomness in the transverse plane were compromised to different extent and hence, the samples exhibited different levels of non-symmetric elastic properties. Determination of the complete stiffness matrix also enabled to determine the Young's modulus, shear modulus and Poisson's ratio of the samples along all directions. These moduli fulfil the thermodynamic constraints imposed by the elastic constants of orthotropic materials. Components of the stiffness matrix obtained using experimental methods show very good correspondence with the predictions from micromechanical models.

Acknowledgements

The authors thank M.J. Hoffmann, R. Oberacker, and T. Waschkies of Insitut für Keramik im Maschinenbau, Karlsruhe Institute of Technology (KIT), Germany, as well as A. Nagel and co-workers at Aalen University of Applied Sciences, Germany, for providing the specimen materials. Financial support from the Deutsche Forschungsgemeinschaft (DFG), Bonn, Germany under projects Wa1122/3-1, Pi785/1-1 and Pi785/1-3 is gratefully acknowledged.

References

[1] N. Chawla, K.K. Chawla, Metal Matrix Composites, Springer Science + Business Media, Inc., New York, USA, 2006.
[2] H. Czichos, T. Saito, L. Smith, Handbook of Materials Measurement Methods, Springer Science + Business Media Inc., Germany, 2006.
[3] E. Schreiber, O.L. Anderson, N. Soga, Elastic Constants and their Measurement, Mcgraw-Hill, Inc., USA, 1973.
[4] M. Radovic, E. Lara-Curzio, L. Riester, Mater. Sci. Eng. A 368 (2004) 56–70.
[5] H. Ledbetter, Mater. Sci. Eng. A 165 (1993) L9–L10.
[6] J.M. Ide, Rev. Sci. Instrum. 6 (1935) 296–298.
[7] L. Landau, E. Lifshitz, Theory of Elasticity, Pergamon, London, 1959.
[8] M.S. King, Int. J. Rock Mech. Min. Sci. Geomech. Abstr. 20 (1983) 237–241.
[9] W.L. Van Heerden, Int. J. Rock Mech. Min. Sci. Geomech. Abstr. 24 (1987) 381–385.
[10] N.A. Al-Shayea, Eng. Geol. 74 (2004) 139–156.
[11] A. Hauert, A. Rossoll, A. Mortensen, Composites Part A 40 (2009) 524–529.
[12] B. Roebuck, T.A.E. Gorley, L.N. McCartney, Mater. Sci. Technol. 5 (1989) 105–117.
[13] T.G. Nieh, D.J. Chellman, Scripta Metall. 18 (1984) 925–928.
[14] J.F. Nye, Physical Properties of Crystals, Oxford Science Publications, USA, 1985.
[15] W.C. Van Buskirk, S.C. Cowin, R.N. Ward, J. Biomech. Eng. 103 (1981) 67–72.
[16] S. Nemat-Nasser, M. Hori, Micromechanics: Overall Properties of Heterogeneous Materials, Elsevier, Holland, 1999.
[17] B. Drach, I. Tsukrov, T. Gross, S. Dietrich, K. Weidenmann, R. Piat, T. Böhlke, J. Solids Struct. 48 (2011) 2447–2457.
[18] J.-M. Gebert, A. Wanner, R. Piat, M. Guichard, S. Rieck, B. Paluszynski, T. Böhlke, Mech. Adv. Mater. Struct. 15 (2008) 467–473.
[19] T. Ziegler, A. Neubrand, S. Roy, A. Wanner, R. Piat, Compos. Sci. Technol. 69 (2009) 620–626.
[20] T. Ziegler, A. Neubrand, R. Piat, Compos. Sci. Technol. 70 (2010) 664–670.
[21] R. Piat, S. Roy, A. Wanner, Key Eng. Mater. 417–418 (2010) 53–56.
[22] R. Piat, I. Tsukrov, N. Mladenov, M. Guellali, R. Ermel, T. Beck, E. Schnack, M.J. Hoffmann, Compos. Sci. Technol. 66 (2006) 2769–2775.
[23] S. Roy, A. Wanner, Compos. Sci. Technol. 68 (2008) 1136–1143.
[24] S. Roy, O. Stoll, K.A. Weidenmann, A. Nagel, A. Wanner, Compos. Sci. Technol. 71 (2011) 962–968.
[25] H.K. Jung, Y.M. Cheong, H.J. Ryu, S.H. Hong, Scripta Mater. 41 (1999) 1261–1267.
[26] M. Koopman, K.K. Chawla, C. Coffin, B.R. Patterson, X. Deng, B.V. Patel, Z. Fang, G. Lockwood, Adv. Eng. Mater. 4 (2002) 37–42.
[27] J.E. Vuorinen, R.B. Schwarz, C. McCullough, J. Acoust. Soc. Am. 108 (2000) 574–579.
[28] H. Ledbetter, C. Fortunko, P. Heyliger, J. Appl. Phys. 78 (1995) 1542–1546.
[29] H. Ogi, K. Takashima, H. Ledbetter, M.L. Dunn, G. Shimoike, M. Hirao, P. Bowen, Acta Mater. 47 (1999) 2787–2796.
[30] L.C. Lynnworth, E.P. Papadakis, W.R. Rea, Ultrasonic measurement of phase and group velocity using continuous wave transmission techniques, AMMRC Report CTR 73-2, January 1973.
[31] A. Wanner, Mater. Sci. Eng. A 248 (1998) 35–43.
[32] J.L. Rose, Ultrasonic Waves in Solid Media, Cambridge University Press, Cambridge, UK, 1999.
[33] J.M. Gebert, B. Reznik, R. Piat, B. Viering, K. Weidenmann, A. Wanner, O. Deutschmann, Carbon 48 (2010) 3647–3650.
[34] J.L. Sarrao, S.R. Chen, W.M. Visscher, M. Lei, U.F. Kocks, A. Migliori, Rev. Sci. Instrum. 64 (1994) 2139–2140.
[35] R.G. Leisure, F.A. Wills, J. Phys.-Condens. Matter 9 (1997) 6001–6029.
[36] A. Migliori, J.L. Sarrao, Resonant Ultrasound Spectroscopy: Applications to Physics, Materials Measurements and Nondestructive Evaluation, John Wiley & Sons, Inc., USA, 1997.
[37] Y. Benveniste, Mech. Mater. 6 (1987) 147–157.
[38] J. Schjødt-Thomsen, R. Pyrz, Mech. Mater. 33 (2001) 531–544.
[39] T.T. Wu, Int. J. Solids Struct. 2 (1966) 1–8.
[40] M. Kachanov, S. Safiro, I. Tsukrov, Handbook of Elasticity Solutions, Kluwer, Netherlands, 2003.
[41] T. Waschkies, R. Oberacker, M.J. Hoffmann, J. Am. Ceram. Soc. 92 (S1) (2009) S79–S84.
[42] R. Piat, Y. Sinchuk, M. Vasoya, O. Sigmund, Acta Mater. 59 (2011) 4835–4846.
[43] ASM International Handbook Committee, Engineered Materials Handbook, vol. 1. Composites, ASM International, 1987.
[44] J.F. Shackelford, W. Alexander, Materials Science and Engineering Handbook, CRC Press, 2001.
[45] B. Huchler, D. Staudenecker, T. Weidler, A. Mattern, A. Nagel, L. Kallien, M. Hoffmann, Proceedings of Symposium Verbundwerkstoffe und Werkstoffverbunde, Frankfurt, Germany, 2005.
[46] S. Roy, J. Gibmeier, V. Kostov, K.A. Weidenmann, A. Nagel, A. Wanner, Acta Mater. 59 (2011) 1424–1435.
[47] G. Garces, G. Bruno, A. Wanner, Acta Mater. 55 (2007) 5389–5400.
[48] CES Edupack, Granta Design Ltd., Cambridge, UK, 2008.
[49] J.-M. Berthelot, Composite Materials: Mechanical Behavior and Structural Analysis, Springer, 1999.
[50] S. Roy, A. Wanner, T. Beck, T. Studnitzky, G. Stephani, J. Mater. Sci. 46 (2011) 5519–5526.
[51] G. Kaplan, T.W. Darling, K.R. McCall, Ultrasonics 49 (2009) 139–142.
[52] S. Roy, B. Butz, A. Wanner, Acta Mater. 58 (2010) 2300–2312.
[53] B.M. Lemprier, AIAA J. 6 (1968) 2226–2227.
[54] R.M. Jones, Mechanics of Composite Materials, Taylor & Francis, Inc., USA, 1999.